

ARTICLE

Ultrafast flavin/tryptophan radical pair kinetics in a magnetically sensitive artificial protein

Received 00th January 20xx,
Accepted 00th January 20xx

Chris Bialas^a, David T. Barnard^b, Dirk B. Auman^a, Rylee A. McBride^b, Lauren E. Jarocha^c, P. J. Hore^c,
P. Leslie Dutton^a, Robert J. Stanley^b and Christopher C. Moser^{*a}

DOI: 10.1039/x0xx00000x

Radical pair formation and decay are implicated in a wide range of biological processes including avian magnetoreception. However, studying such biological radical pairs is complicated by both the complexity and relative fragility of natural systems. To resolve open questions about how natural flavin-amino acid radical pair systems are engineered, and to create new systems with novel properties, we developed a stable and highly adaptable *de novo* artificial protein system. These protein maquettes are designed with intentional simplicity and transparency to tolerate aggressive manipulations that are impractical or impossible in natural proteins. Here we characterize the ultrafast dynamics of a series of maquettes with differing electron-transfer distance between a covalently ligated flavin and a tryptophan in an environment free of other potential radical centers. We resolve the spectral signatures of the cysteine-ligated flavin singlet and triplet states and reveal the picosecond formation and recombination of singlet-born radical pairs. Magnetic field-sensitive triplet-born radical pair formation and recombination occurs at longer timescales. These results suggest that both triplet- and singlet-born radical pairs could be exploited as biological magnetic sensors.

Introduction

In biology, free radicals form and decay through the transfer of single electrons between redox cofactors (e.g. flavins¹, tetrapyrroles² and metal clusters³), amino acids (e.g. Trp, Tyr and Cys)⁴ and substrates (e.g. O₂⁵, NO⁶, and ribonucleotides⁷). Their action supports vital functions (respiration⁸, DNA repair⁹, and photosynthesis¹⁰) and destructive processes linked to health problems (formation of reactive oxygen species and DNA damage)^{8,11}. Light-activation of cofactors is an important means of creating radical pairs (Figure 1). In the photoreceptor cryptochrome, a blue-light activated flavin (FAD) cofactor oxidizes a chain of three tryptophans resulting in a radical pair composed of a singly-reduced semiquinone flavin and an oxidized tryptophan¹². The singlet/triplet spin dynamics of the FAD^{•−}/Trp^{•+} radical pair have been proposed as the source of cryptochrome sensitivity to the Earth's magnetic field in the context of animal navigation^{13,14}.

Unfortunately, measurements of magnetic field effects on cryptochrome radical pairs are complicated by several technical difficulties: purifying adequate amounts of the relatively unstable natural proteins; performing extensive mutagenesis

without disrupting the protein fold; and the unrestrained reactivity of the radicals themselves^{15,16}. These challenges can be overcome by preparing and characterizing radicals in the controlled environment of artificial protein maquettes^{17, 18, 19}. Maquettes are simple, stable, and mutation-tolerant four-helical bundles that can be expressed in high yield from *E. coli* using standard methods²⁰. This system offers superior design control over natural proteins and possesses greater biological relevance than non-protein analogues. In this work, we employ a family of maquettes that vary the separation of a flavin/Trp radical pair from near contact to ~17 Å.

Previous studies with microsecond time resolution demonstrated that maquettes with a flavin/Trp separation of < 11.2 Å, produced photo-excited radical pairs that display magnetic field-sensitivity at millitesla field strengths under ambient conditions^{17,18}. These magnetic field effects clearly arose from a radical pair formed from an excited triplet state flavin precursor. However, as the efficiency of quenching of the flavin fluorescence decreased with increasing flavin/Trp spacing, we hypothesized that the quenching mechanism was electron transfer from the flavin singlet state^{17,18}. Ultrafast studies are needed to resolve the excited-state quenching mechanism and, more importantly, the roles played by possible singlet- and triplet-born radical pairs in order to uncover the design rules to construct biologically based efficient magnetic field-sensing radical-pair systems.

^a Johnson Research Foundation, Department of Biochemistry and Biophysics, University of Pennsylvania, Philadelphia, Pennsylvania 19104, United States.

^b Department of Chemistry, Temple University, Philadelphia, Pennsylvania 19122, United States.

^c Department of Chemistry, University of Oxford, Physical and Theoretical Chemistry Laboratory, Oxford OX1 3QZ, United Kingdom.

† Footnotes relating to the title and/or authors should appear here.

Electronic Supplementary Information (ESI) available. See DOI: 10.1039/x0xx00000x

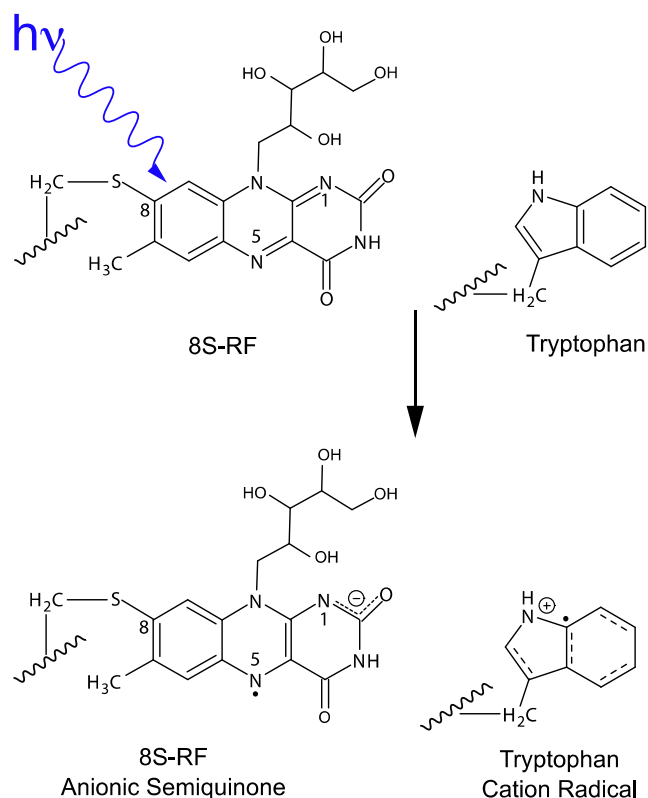


Fig. 1. A cysteine covalently couples riboflavin at position 8. Upon excitation with blue light, the flavin oxidizes a nearby tryptophan to form a radical pair comprising the flavin anion semiquinone radical and tryptophan cation radical.

Methods

Materials

All materials were purchased from Sigma Aldrich.

Maquette Preparation

Four-helix bundle protein maquettes with a 6-histidine tag were designed, expressed, purified and prepared as described elsewhere¹⁸. Briefly, the maquette sequence was encoded onto a plasmid and overexpressed from *E. coli*. After cellular disruption and Ni column purification of the tagged maquette, the tag was removed using a tobacco etch virus protease. The protein was concentrated to ~0.5 mM, flavinated by reacting with 8-bromo-riboflavin¹⁸, purified via reverse phase HPLC and stored as a lyophilized powder. The powder was reconstituted in buffer (200 mM KCl, 20 mM KH₂PO₄, pH 7.5), to a concentration of ~50–100 μM flavomaquette ($\epsilon_{475\text{ nm}} = 24,640\text{ M}^{-1}\text{ cm}^{-1}$), and purged for 30 min with high purity Ar scrubbed through a train of reduced VOSO₄ solutions to remove residual O₂²¹. The sample was then passed through a 0.22 μm syringe filter in an anaerobic glove box to remove aggregates.

Transient Absorption Spectroscopy

Broadband (425–715 nm) pump-probe femtosecond transient absorption spectra were recorded as described elsewhere²². The samples were placed in a quartz cuvette (Spectrocell FUV R-3002-T, 2 mm path length, internal dimensions 2×2×45 mm) and maintained at 25 °C using a temperature-controlled cuvette holder (QNW FLASH 300)

under continuous stirring with an 8 mm diameter by 0.6 mm thick magnetic stirrer disc. Spectra were also collected from 340 to 600 nm at temperatures of 5 and 37 °C. Samples were interrogated by a Ti:sapphire regenerative amplifier consisting of a Ti:sapphire oscillator (KLM, ~80 MHz, 840 nm) pumped by a 532 nm Nd:YAG (neodymium-doped yttrium aluminium garnet) laser amplified using a regenerative amplifier to produce ~200 μJ, 120 fs pulses at ~250 Hz. This train of pulses was split into two beams to produce a white-light continuum probe (WLC) and a pump. The WLC was generated by focusing the beam into a slowly translating CaF₂ crystal. The 840 nm pump beam was frequency-doubled to 420 nm by second harmonic generation in a 2 mm type-I BBO crystal.

The pump was mechanically chopped at 125 Hz and focused with a 40 cm quartz lens, while the WLC was focused using an off-axis 90° aluminium parabolic mirror (focal length 10 cm). The angle between the focused pump and probe beams was ~2° at the sample. Their relative polarization was set to the magic angle (54.7°) using a half-wave plate in the pump beam. A CMOS camera (Mightex) with 6 μm square pixels was placed at the focus to measure the diameters of the focused beams. This was to ensure that the entire probed region was covered by the pump. The optical alignment of the motorized pump delay stage was checked to ensure overlap over the full 3.2 ns range. Typical pump and probe beam diameters were 264 and 126 μm.

Remaining near-IR fundamental components in the WLC were removed with a Schott BG39 and liquid NiSO₄ filters. Pump power was measured before and after the completed scans by reflecting the pump pulse before the cuvette onto a calibrated silicon joulemeter (Molelectron J3-S10), read by a 400 MHz digital oscilloscope (Rigol). The WLC was dispersed in a 0.25 m spectrograph with ~4 nm bandpass (Digikrom 240i). The signal was detected using a –40 °C cooled CCD detector (Andor, 1024×32 pixels) at ~250 Hz. The system was controlled using an in-house developed LabView program. Data were taken as an average of 5 scans every 0.7 nm from 200 fs to 3.5 ns, on a log time scale by averaging 400 spectra per scan.

Data Analysis

Data were analysed using Matlab 2015b (MathWorks), Origin 8.1 SR 3 (Origin Lab Corporation), and Mathematica 9 (Wolfram). Five pre-zero spectra were used as a background correction along with a dark bias current. Chirp effects were minimized by discarding data with delays between 0 and 1 ps. The data were smoothed using an adjacent averaging filter (5-point window) and normalized to the absorption at the earliest stable time point (bleach: 1 ps; triplet and stimulated emission: 25 ps). A 20 nm bin was selected about each wavelength of interest. Data were fit to single or double exponential functions using functions built into Origin 8.1 SR 3.

The smoothed light-induced difference spectra at a range of times were also analysed using global fit analysis^{23,24} with an in-house script written in Mathematica 9. The dimensionality of the data was reduced using the singular value decomposition (SVD) function and then fit to first-order kinetic models, using the FindMinimum function.

Results

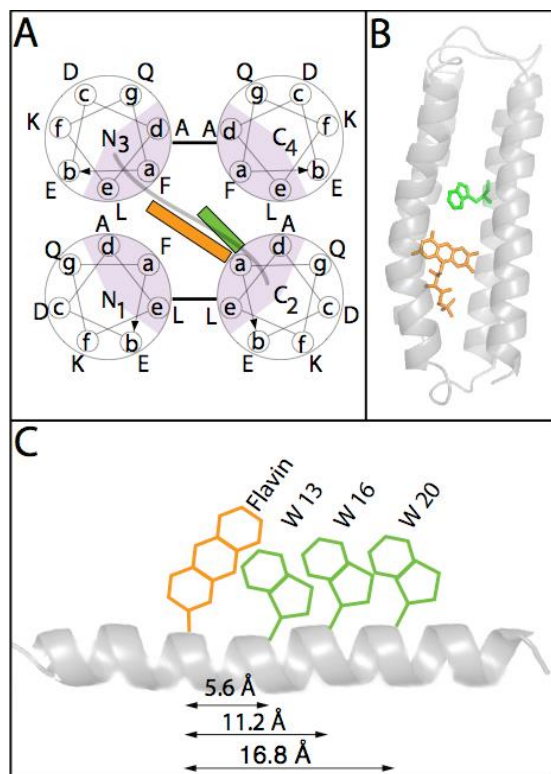


Fig. 2 Schematic representation of flavomaquette designs. A) Plan view of the binary patterning of the four-helical bundle. The outside is composed of hydrophilic amino acids (white) while the core contains hydrophilic amino acids (purple shading) as well as a cysteine which ligates riboflavin (orange rectangle) and the tryptophan (green rectangle). The helices are arranged antiparallel to one another and linked together by flexible serine/glycine loops. B) Side view of a cartoon of the W16 maquette showing the helices as well as riboflavin (orange) and the tryptophan (green). C) Cartoon highlighting the distance as measured between the C_β atoms of the ligating cysteine and of the tryptophan as a proxy for the edge-to-edge tunnelling distance.

Results

We report the ultrafast dynamics of a family of four flavomaquettes. The designs differed only in the presence or position of a tryptophan (Figure 2). Care was taken to exclude other possible radical-forming amino acids such as tyrosine and histidine from the sequence. Each design contained a cysteine-ligated riboflavin (8S-RF) at the buried 9th position (heptad position “a”) of the second helix. A Trp-free variant contained no tryptophan, while variants W13, W16, and W20 contained a tryptophan on the same helix at buried positions 13, 16, and 20, respectively (heptad positions “a” or “d”). In tryptophan-containing maquettes, the distances between the β carbons (C_β) of the 8S-RF and the tryptophan are 5.6 Å for W13, 11.2 Å for W16 and 16.8 Å for W20 (Figure 2C).

Transient spectra recorded between 425 nm and 715 nm at delay times of 0.2 ps to ~3.5 ns at 25 °C are shown in Figure 3. The spectra are dominated by two negative transients (450 nm and 560 nm) and three positive transients (500 nm, 525 nm, and 700 nm) in all designs. Assignment of these transients to excited electronic states of 8S-RF begins with the simpler Trp-free maquette (Figure 3D). Direct ligation of the cysteine to the flavin ring at the 8-position systematically alters the spectroscopic

properties compared to free riboflavin²⁵ as the Cys sulfur orbitals mix with the relevant flavin orbitals (Figure 1). Figure 3E shows the greater steady-state absorption in the shoulder of the $S_0 \rightarrow S_1$ transition (475 nm). The ground state absorbance of the Trp variants show slight differences in the vibronic structure¹⁸, which are reflected in the initial bleach signal. Compared to FMN, this flavin has sharper,

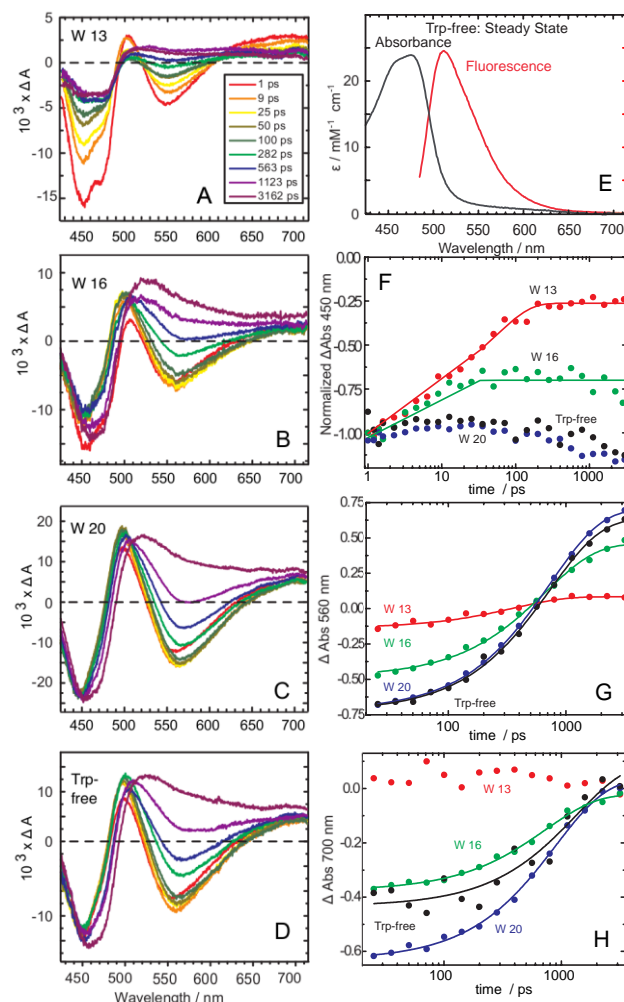


Fig. 3 Time-resolved transient absorption spectra of the flavomaquettes. A through D) 8S-RF was excited at 420 nm using a fs Ti:sapphire laser. Each trace represents the spectrum observed at the delay time after excitation indicated in the inset. Panels A through D describe W13, W16, W20 and the Trp-free maquettes, respectively. The pump beam scatter has been removed for clarity. E) The steady state absorption extinction coefficient and relative fluorescence of the Trp-free maquette. F) The time evolution of the flavomaquette bleach plotted on a log time scale. Time points were taken from 1 ps to ~3.2 ns in a 20 nm window about 450 nm (440 to 460 nm) for W13 (red), W16 (green), W20 (blue) and the Trp-free (black). Data were normalized between samples to the GSB amplitude. W13 was fit with a double exponential while W16 was fit with a single exponential. W20 and the Trp-free could not be reliably fit with either function. G) The time evolution of the 8S-RF stimulated emission plotted on a log time scale. Time points were taken from 25 ps to ~3.2 ns in a 20 nm window about 560 nm for W13 (red), W16 (green), W20 (blue) and the Trp-free (black). Absorbance change was normalized relative to each design's ground state bleach (440-460 nm) at 1 ps. All series were fit with single exponentials (solid lines). H) The time evolution of the 8S-RF triplet feature plotted on a log time scale. Time points were taken from 25 ps to ~3.2 ns in a 20 nm window about 700 nm (690-710 nm) for W13 (red), W16 (green), W20 (blue) and the Trp-free (black). Absorbance change was normalized relative to each design's ground state bleach (440-460 nm) at 1 ps. All but W13 were fit with single exponentials. W13 could not be reliably fit with an exponential function. The fitting parameters are summarized in Table 1.

blue-shifted singlet excited state absorption and stimulated emission²⁶.

This report is the first ultrafast study of 8S-RF and relies on assignment of spectral features by comparison with the ultrafast spectra of FMN^{26,27}, FAD²⁸ and cryptochrome^{28,29,30}. The persistent, negative signal centered at ~450 nm of the Trp-free design (Figure 3D) is attributed to the ground state bleach (GSB). At the earliest time points this bleach band is narrowed and blue-shifted. At 560 nm, a negative signal was observed that red-shifted after ~10 ps and eventually crossed zero between 0.5 and 1 ns. Transients in this wavelength region include both singlet stimulated emission (SE) and triplet absorption. The broad absorbance feature at 700 nm, clearest at ~3.2 ns, was attributed to the 8S-RF triplet²⁶.

Selected wavelength kinetic analysis

While these transient absorption features were comparable in all four designs, their time evolution varied significantly. The simplest kinetic analysis involves selecting wavelengths that are dominated by the major difference absorbance features. The absorbance changes at 450 nm monitored the flavin GSB (Figure 3F). Excited singlet SE was examined at 560 nm. (Figure 3G). The excited triplet absorbance was monitored at 700 nm (Figure 3H). In both Trp-free and W20 maquettes, little GSB recovery was observed in the first 50 ps (< 10%, Figure 3F). The broadening and red-shift of this bleach signal is attributed to the decay of the excited singlet state absorption (Figure 3A-D). In W16, the GSB had a similar broadening and red shift along with a ~25% single exponential recovery ($\tau = 5$ ps) that remained stable after ~30 ps. In W13, the GSB was the broadest and most closely resembled the steady state absorbance. The GSB recovered ~75% as a double exponential ($\tau_1 = 5$ ps, relative amplitude = 0.42; $\tau_2 = 60$ ps, relative amplitude = 0.58) that remained stable after ~200 ps.

The SE feature underwent a 5 nm red-shift from 555 nm to 560 nm in the first 10 ps (Figure 3A-D). The red shift was most obvious in the Trp-free and W20 maquettes, but still observable in W16 and W13. 420 nm laser excitation is about 50 nm blue of the flavin $S_0 \rightarrow S_1$ absorption maximum (Figure 3E) and appears to create a hot singlet state that vibrationally relaxes on this timescale. The SE transient, a proxy for singlet decay, was slowest in the Trp-free maquette ($\tau = 734$ ps), followed by W20 ($\tau = 736$ ps), W16 ($\tau = 663$ ps) and fastest in W13 ($\tau = 357$ ps, Figure 3G).

The triplet transient formation roughly mirrored the singlet decay for all maquettes but W13 (Figure 3H). Formation was slowest in the Trp-free ($\tau = 1300$ ps), followed by W20 ($\tau = 890$ ps), and fastest in W16 ($\tau = 730$ ps). W13 did not show significant change and could not be fit.

Singular Value Decomposition (SVD) global analysis

To complement the analysis of individual wavelengths and resolve the multiple spectrally overlapping components, full data sets (intensities over all times and wavelengths) were fit using a global SVD analysis. The magnitudes of the SVD singular values indicate three to four spectrally and kinetically distinct

components above the background noise (Figure S1). Fitting of the dimensionally reduced data to a four-state sequential kinetics model shows that the first state transitioned rapidly ($\tau < 10$ ps) to the second state, and the second state to the third state ($\tau \approx 0.8$ ns; Figure 4). Conversions of any of the three states to a spectrally silent fourth state required fitting to time constants (τ) outside of the experimental window (~3.2 ns) of the instrument. The four components were assigned to the following species: vibrationally hot flavin singlet ($^1F^*_{\text{hot}}$), vibrationally relaxed flavin singlet ($^1F^*_{\text{cool}}$), flavin triplet ($^3F^*$), and ground state (F). There is little evidence of the absorption

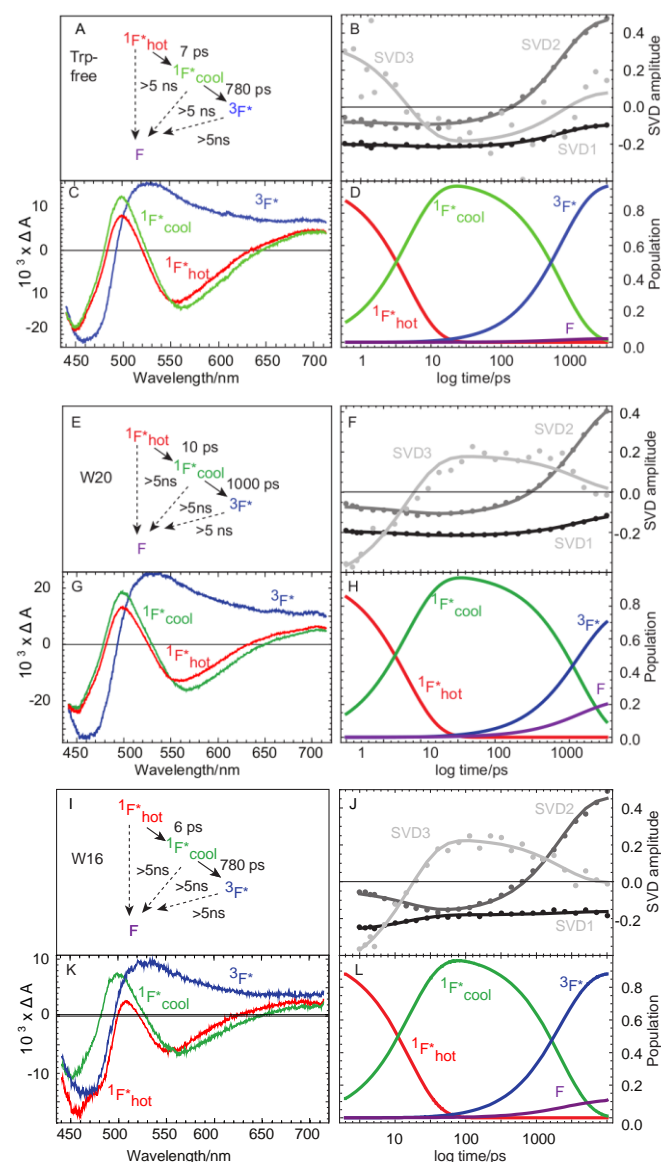


Fig. 4 SVD global analysis fit to a four-state sequential model. Top A-D) The Trp-free maquette. Middle E-H) W20, and Bottom I-L) W16. A, E, I) The kinetic model used to fit the data. Reaction times are shown next to arrows. Fluorescence and phosphorescence rates are not well defined on this timescale. B, F, J) Log time dependence of the three principal SVD components (circles) and their fits to the kinetic model (lines). C, G, K) Model fit difference spectra relative to the ground state. D, H, L) Time course of the model populations. Reduced χ^2 for Trp-free, W20 and W16 are 1.3, 1.0 and 1.1, respectively.

Design	Bleach 450 nm [r^2] τ / ps	SVD $^1F^*_{\text{hot}} \rightarrow \text{cold}$ τ / ps	Stimulated Emission 560 nm [r^2] τ / ps	Triplet 700 nm [r^2] τ / ps	SVD $^1F^*_{\text{cold}} \rightarrow ^3F^*$ τ / ps
Trp-free	No Fit	7	734 ± 32 [0.99]	1300 ± 470 [0.93]	780
W 20	No Fit	10	736 ± 10 [0.99]	890 ± 45 [0.99]	1000
W 16	5 ± 1 [0.89]	6	663 ± 33 [0.99]	730 ± 45 [0.99]	780
W 13	5 ± 2 , 48% 60 ± 10 , 52% [0.99]	10	357 ± 53 [0.97]	No Fit	790

Table 1. Single wavelength fit kinetic parameters for ground state bleach, stimulated emission, molecular triplet excited state in the flavomaquettes, with r^2 coefficient for quality of fit. The corresponding SVD fit kinetic parameters apply to a sequential model except for $^1F^*_{\text{cold}} \rightarrow ^3F^*$ in W13, which applies a parallel model (figure 5).

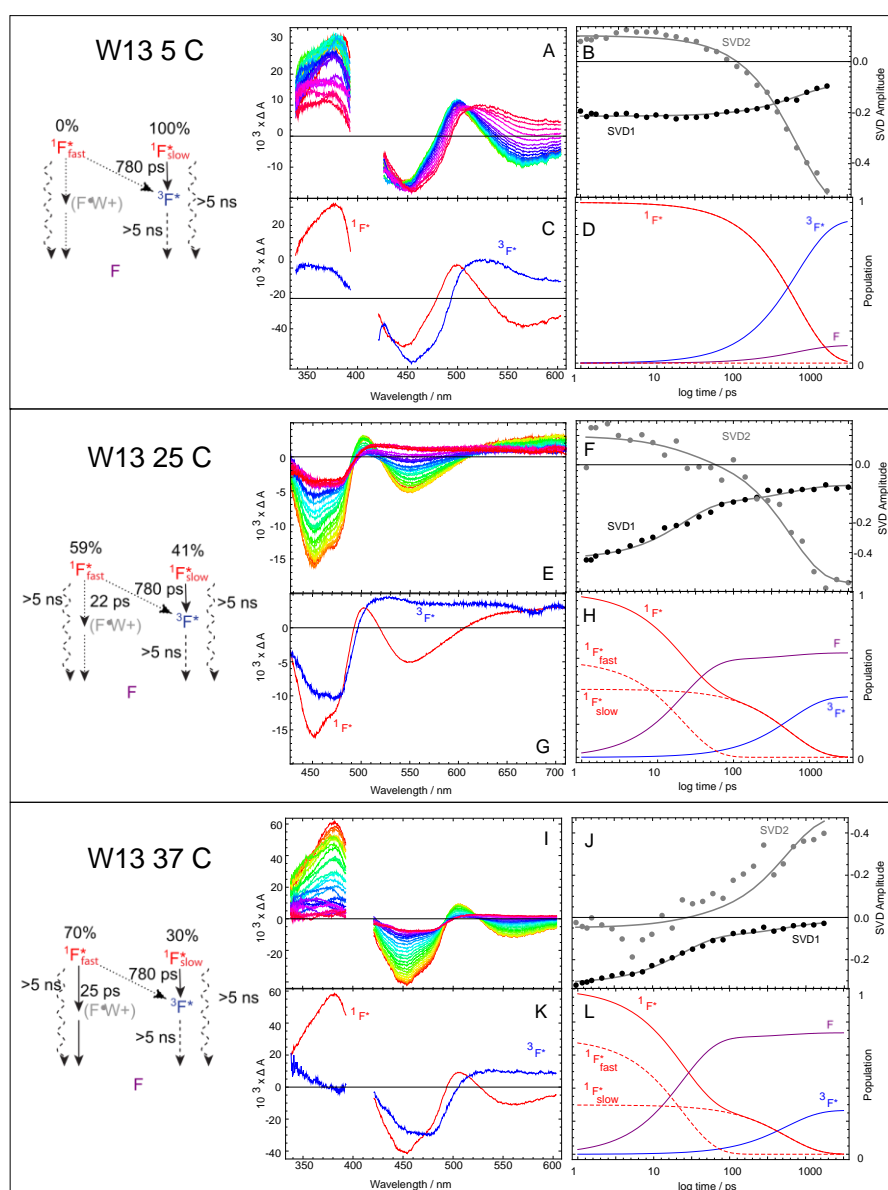


Fig. 5 SVD global analysis fit analysis of W13 according to a 4-state parallel model at three different temperatures and spectral ranges. Top A-D) W13 at 5 °C, Middle E-H) W13 at 25 °C, and Bottom I-L) W13 at 37 °C. Left Panels) The elementary parallel kinetic model used to fit W13. Here two excited singlet state populations ($^1F^*_{\text{fast}}$ and $^1F^*_{\text{slow}}$) evolve

separately: one to the ground state (F), presumably through rapid forward and reverse electron transfer; another to the triplet populations are indicated. A,E,I) The time resolved spectra used for fitting. B,F,J) The time evolution of the amplitude of the three SVD spectral components (dots) with the parallel kinetic model fits (lines). Reduced $\chi^2 =$

1.1. C,G,K) The model-derived spectra of the parallel system for the excited singlet (red) and triplet (blue) states. D,H,L) Model population of the three states in log time.

due to oxidized tryptophan in this spectral region³¹. Nor is there spectral evidence of a flavin semiquinone in the UV spectra collected at 5 and 37 °C (Figures 5, S2-S5).

A homogeneous four-state sequential kinetic model is adequate to describe the data in the Trp-free, W20 and W16 maquettes. However, it clearly fails to fit the third SVD component of W13 (lightest grey in upper right panel of Figure S2). Furthermore, the SVD-derived relative extinction coefficients for the flavin ground state bleach of the cool singlet and triplet spectra (Figure S2) appear unreasonably small. This suggests that for the maquette design with the shortest distances between excited flavin and tryptophan, there is significant excited singlet state quenching (for example by electron transfer) in competition with intersystem crossing to the triplet state. Yet the persistence of a triplet spectral signal at 1 ns indicates that a substantial fraction of the excited singlet nevertheless survives on the timescale of intersystem crossing. SVD model fitting with an elementary parallel model having two populations of maquettes (one capable of sub-ns electron transfer and one not), provides an adequate fit to the spectral data with more appropriate extinction coefficients for the ground state bleach (Figure 5). In this model the intersystem crossing rate is fixed at the rate measured for the Trp-free maquette (Figure 3F), while the rate of electron-transfer quenching and the fraction of ultrafast electron-transfer active and inactive populations were fit. On the basis of the quantum yield of triplet state, the rate of singlet internal conversion and fluorescence is expected to be slower than the time scale of the measurements, ~5 ns. For the rapid electron-transfer-competent population, the fitted electron transfer time of 25 ps would correspond to an edge-to-edge electron tunneling distance of ~6.9 Å³². The back electron transfer to the ground state, which has a large driving force, is also expected to be fast, leading to little spectral accumulation of any intermediate charge-separated state. An edge-to-edge separation of ~10 Å or more for the slow population would favor intersystem crossing and suppress electron transfer on this timescale.

Only W13 shows temperature sensitive dynamics (Figure 5, S2-S5). Raising the temperature to 37 °C slightly increases the degree of singlet quenching; however, lowering the temperature of W13 substantially suppresses singlet state quenching leading to a much larger yield of triplet conversion (Figure 5). Apparently, lowering the temperature largely disables the motions that enable flavin and tryptophan to enter rapid electron-transfer range.

DISCUSSION

De novo designed maquettes provide a unique opportunity to study flavin/Trp radical pairs in a controlled environment. Maquette design freedom enables us to vary the distance between radical pair members in order to understand the effect on the rate of formation/decay and spin dynamics.

Kinetic analysis of the time traces together with the global fit of the broad spectral changes in the Trp-free control maquette support a homogeneous four-state kinetic model with three distinct difference spectra. The first state, identified as a hot excited singlet rapidly relaxes ($\tau = 7 \pm 2$ ps) to a second state, identified as a red-shifted and vibrationally-cooled singlet. This evolution shows a similar extent and timescale to other flavin systems^{28,33}. The expected transition to a third state, the triplet, at 1.0 ± 0.3 ns is faster than the ~6 ns intersystem crossing (ISC) rate of non-covalently bound FMN³⁴. The faster ISC is similar to that of flavins found in LOV domains^{35,36}. In both cases the spin-orbit coupling between the flavin's ring system and a nearby or attached cysteine sulfur (heavy atom effect) is believed to accelerate the ISC³⁷.

As expected, the maquette design W20, with the greatest flavin/Trp separation resembled the Trp-free control maquette both in the single-wavelength kinetic analysis and during the global fitting. With an edge-to-edge donor/acceptor distance similar to the C _{β} separation of ~16.8 Å and a driving force of roughly -1.2 eV, electron tunneling between the cofactors should be on the microsecond timescale (Figure 6)²⁵, too slow to be observed in these measurements.

W16, on the other hand, provides evidence for radical pair kinetics on the ultrafast timescale. Given the near identical biophysical properties across all designs save for the tryptophan-8S-RF distance, electron transfer is the most plausible mechanism to explain the ~25% recovery of the GSB. However electron transfer over ~11.2 Å, estimated from the distance between the C _{β} atoms of Cys and the tryptophan, should be slower than the 3.5 ns window of this experiment³⁵. In accordance with longer timescale transient spectroscopy¹⁸, we propose that protein fluctuations slower than 100 ns modulate the distance between the redox centers. Considerable protein motions that reorganize redox active amino acids or cofactors are known to affect electron-transfer rates in flavoprotein BLUF domains³⁸ and may also be in play in FAD-dependent DNA photolyase^{39,40}. Molecular dynamics simulations predict similar motion in *Arabidopsis* cryptochrome

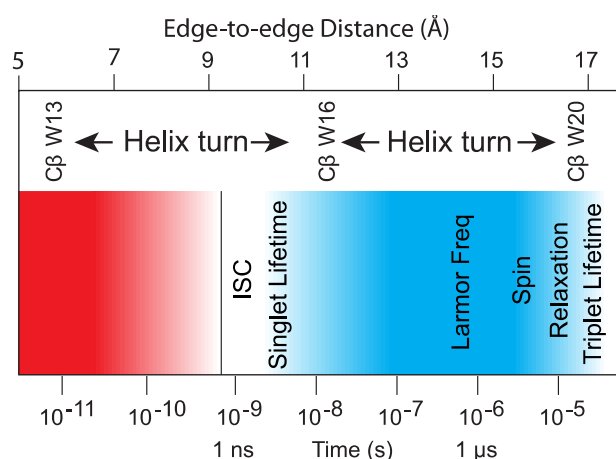


Fig. 6 Characteristic times for flavomaquette kinetics. The expected characteristic timescales for electron tunnelling between 8S-RF and Trp for various designs are based upon the distances between β -carbons of the flavin-ligating cysteine and the tryptophan with a driving force of ~-1.2 eV. Other important timescales are the singlet decay

lifetime, 8S-RF ISC time constant (both determined in this study), 8S-RF triplet decay lifetime¹⁸, Larmor frequency of an Earth-strength magnetic field which modulates singlet/triplet conversion, and the upper limit of the spin correlation time required for magneto-sensitive radical pairs sensitive to the Earth's magnetic field³⁰.

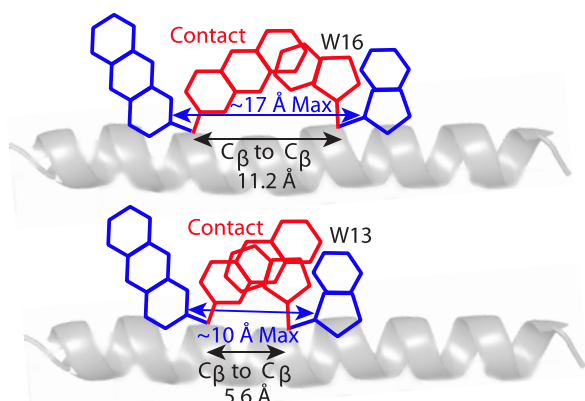


Fig. 7 Conformational modulation of riboflavin/tryptophan distances in flavomaquettes. In this example, W16 has an 11.2 Å estimated distance between the C β atoms of the ligating cysteine and the tryptophan. However, since the redox-centre dimensions of ~8 and ~5 Å for 8S-RF and Trp, respectively, are comparable to the C β anchor-point separation, it is plausible to adopt conformations from van der Waals contact to ~17 Å edge-to-edge distance. Corresponding maximum and minimum distances for W13 are ~10 Å and van der Waals contact.

and photolyase^{39,41}. With redox center dimensions of 8 and 5 Å for the riboflavin and tryptophan respectively, rotations about the beta carbons could in principle sample donor-acceptor edge-to-edge distances from van der Waals contact to ~17 Å (Figure 7). A 5 Å change in distance between flavin and Trp is sufficient to change electron-tunneling rates 1000-fold (Figure 9). Therefore, in W16, only the population of flavin-Trp pairs with less than ~10 Å separation would be able to transfer electrons to the singlet state on the ultrafast timescale before intersystem crossing to the triplet. Subsequent charge recombination over the same distance with a similar driving force will also be rapid with little spectral accumulation of this intermediate. Maquettes with more distant redox centres would evolve unperturbed to the triplet state.

Previous cryptochrome work suggested that faster than expected electron transfer for a given distance could reflect a frequency-dependent dielectric response that modulates reorganization energy⁴². However, in the case of W13 with a large driving force for electron transfer between flavin and Trp, a decrease in reorganization energy would slow rather than speed electron transfer and cannot explain the observed electron-transfer rates.

Evidence for singlet radical pair formation and conformational heterogeneity is clearest in W13 at 25 °C. The GSB recovery kinetics of Figure 3F and the parallel SVD kinetic model of Figure 5 support the view that the closer anchoring of flavin and tryptophan on the helical backbone enables ~60% of the electron transfer to occur from the singlet state, consistent with observed GSB recovery. The characteristic rate of excited singlet decay of this population indicates a ~6.9 Å edge-to-edge tunnelling distance, given a typical reorganization energy of

around 0.9 eV³². This distance is in the middle of the range for the possible rotational conformers for flavin and Trp (Figure 7).

On a slower timescale, electron transfer from the triplet state can form a longer-lived, magnetically sensitive radical pair. This triplet radical pair can undergo de/protonation reactions¹⁷, form a singlet radical pair or recombine, as summarized in Figure 8. To suppress rapid electron transfer on the timescale of intersystem crossing in this population, a rotational conformation of flavin and the Trp at position 13 would need to approach the long-distance extreme of ~10 Å (Figure 7). This is apparently the protein packing geometry that is favoured when the temperature is dropped to 5 °C. However, additional studies are required to investigate this hypothesis.

Despite early evidence supporting a triplet-born radical pair in cryptochrome⁴³, to date, all magnetically sensitive radical pairs in cryptochromes are singlet-born¹³. Chemically synthesized systems often show magnetically sensitive triplet-born radical pairs^{44,45}. Maquette constructs show that both singlet- and triplet-born flavin/amino acid radical pairs can be achieved in a protein environment and suggest that a broader search of natural systems might uncover triplet-born radical pairs.

The dominance of singlet-born cryptochrome radical pairs may reflect an evolutionary legacy from photolyase-like precursor designs⁴⁴ relying on FAD as the light-activated cofactor. As a cofactor, FAD carries the inherent “threat” of unproductive electron transfer from the adenine ring to the excited flavin nucleus when in the “stacked” conformation domains^{33,46}. This may lead to selective pressure to maintain a Trp residue in near contact with the flavin nucleus to support rapid, productive electron transfer to the excited flavin singlet state and avoid adenine electron transfer that quenches

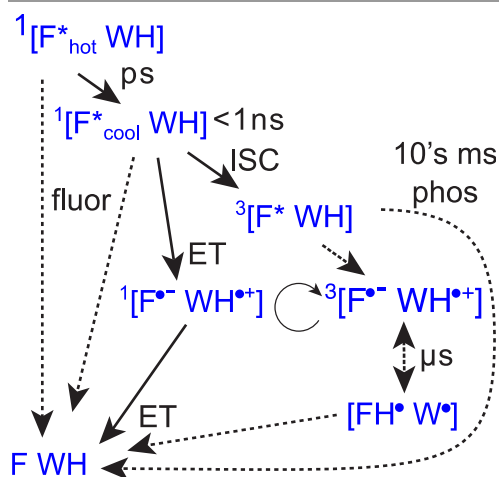


Fig. 8 A kinetic model of the dynamics and electron transfer (ET) in flavomaquettes. The flavin absorbs a photon to form a hot excited singlet state that cools in ps. Depending on the separation between flavin and tryptophan, the singlet may undergo electron transfer to create a singlet-born radical pair or undergo intersystem crossing in less than 1 ns to the triplet with a concomitant loss of fluorescence. The triplet-excited flavin may form a triplet-born radical pair or phosphoresce if the tryptophan is too distant. Triplet-born radical pairs can interconvert between the singlet and triplet state in a magnetic field-dependent fashion. Singlet radical pairs can charge-recombine, while triplet radical pairs may persist long enough for microsecond (de)protonation¹⁷.

flavin/distant Trp radical pair formation. This is not an issue for the adenine-free FMN in natural flavoproteins containing LOV domains or for the 8S-RF in maquettes. A survey among natural FMN-binding proteins may uncover unsuspected triplet-born radical pair dynamics in natural systems. With a less powerful photooxidant, triplet-born radical pair systems may be less prone to unproductive, off-pathway electron-transfer reactions, well-demonstrated in photolyase⁴⁶.

Conclusions

Maquettes offer a robust and adaptable test bed for manipulating radical pair lifetimes with a view towards enhancing magnetic field sensitivity and directional sensing. Designs placing two Trps at close and intermediate positions in an electron transfer relay should facilitate production and stabilization of both singlet- and triplet-born radical pairs, especially when a redox-potential gradient is introduced by varying the solvent exposure of the Trps, similar to that seen in natural cryptochrome chains (Figure S6). It is also reasonable to substitute non-Trp electron donors with smaller or larger hyperfine interactions to test predicted changes in magnetic field sensitivity^{45,47}. This includes flavin/tyrosine radical pairs invoked in some natural proteins^{48,49,50}. We are presently addressing these questions by characterizing maquettes with alternative flavins, flavin/tyrosine pairs, as well as maquettes that offer quinone, methionine and histidine alone and in combination as radical-pair partners (Figure S7). Finally, experiments using polarized light and/or oriented samples are underway to more rigorously investigate Trp orientation in these systems.

Conflicts of interest

There are no conflicts to declare.

Acknowledgements

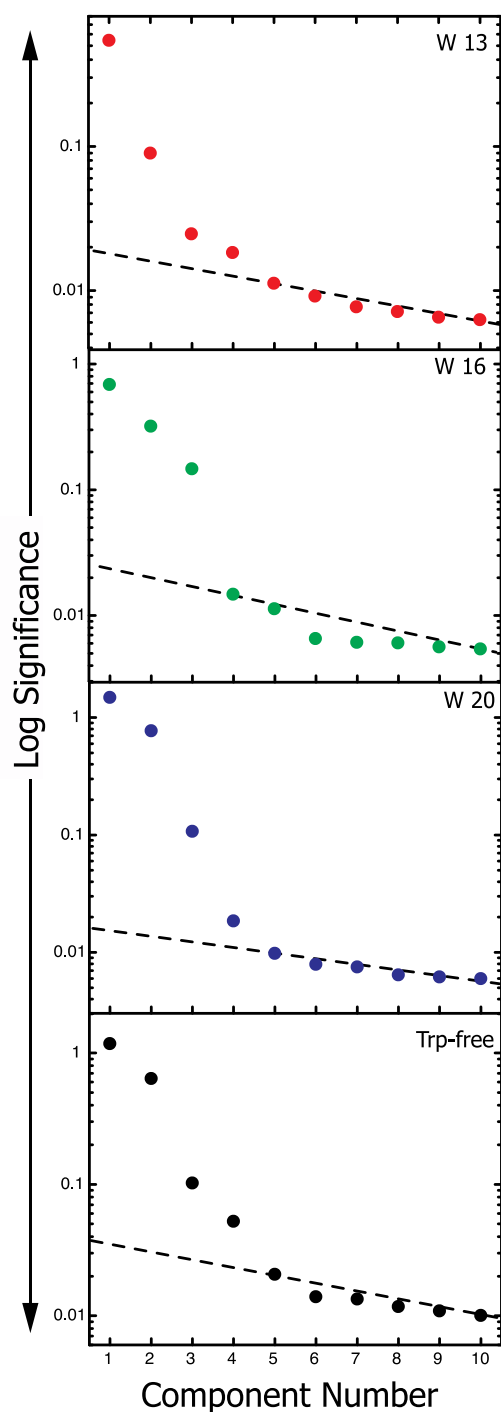
We are grateful to the following for financial support: the European Research Council (under the European Union's 7th Framework Program, FP7/2007-20013/ERC Grant Agreement No. 340451 to PJH). DTB, RAM, and RJS acknowledge funding from the NASA Exobiology Program (Grant 80NSSC17K0033). CB would like to thank S.A. Vinogradov and A. Cember (Biochemistry and Molecular Biophysics Department at the Perelman School of Medicine at the University of Pennsylvania) for useful discussion and M. Leonard for assistance in making graphics (Biomedical Art and Design at the Perelman School of Medicine at the University of Pennsylvania). LEJ thanks Christiane Timmel and Stuart Mackenzie for support and encouragement.

Notes and references

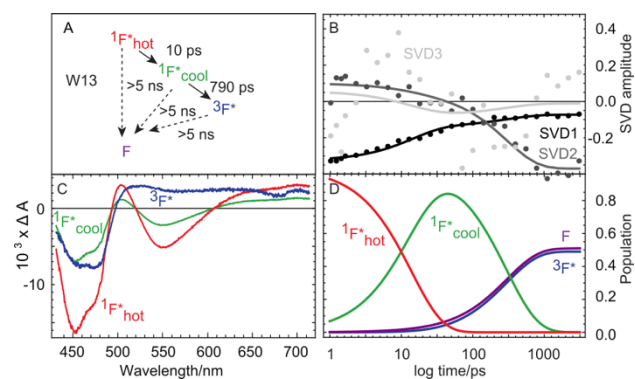
- 1 F. Muller, *Free Radic. Biol. Med.*, 1987, **3**, 215–230.
- 2 I. Matsunaga and Y. Shiro, *Curr Opin Chem Biol*, 2004, **8**, 127–132.
- 3 N. Yang, M. Reiher, M. Wang, J. Harmer and E. C. Duin, *J. Am. Chem. Soc.*, 2007, **129**, 11028–11029.
- 4 S. L. Winder, R. W. Broadhurst and P. J. Hore, *Spectrochim. Acta, Part A*, 1995, **51**, 1753–1761.
- 5 M. Hayyan, M. A. Hashim and I. M. AlNashef, *Chem. Rev.*, 2016, **116**, 3029–3085.
- 6 R. Palmer, A. G. Ferrige and S. Moncada, *Nature*, 1987, **327**, 524–526.
- 7 P. Reichard and A. Ehrenberg, *Science*, 1983, **221**, 514–519.
- 8 H. Nohl, *Ann Biol Clin (Paris)*, 1994, **52**, 199–204.
- 9 J. Yamamoto, P. Plaza and K. Brettel, *Photochem. Photobiol.*, 2017, **93**, 51–66.
- 10 S. V. Feskov, V. A. Mikhailova and A. I. Ivanov, *J. Photochem. Photobiol., C*, 2016, **29**, 48–72.
- 11 J. Juutilainen, M. Herrala, J. Luukkonen, J. Naarala and P. J. Hore, *Proc. Roy. Soc. B.*, 2018, **285**.
- 12 M. Ahmad, *Curr. Opin. Plant Biol.*, 2016, **33**, 108–115.
- 13 P. J. Hore and H. Mouritsen, *Annu. Rev. Biophys.*, 2016, **45**, 1–48.
- 14 T. Ritz, S. Adem and K. Schulten, *Biophys. J.*, 2000, **78**, 707–718.
- 15 K. Maeda, A. J. Robinson, K. B. Henbest, H. J. Hogben, T. Biskup, M. Ahmad, E. Schleicher, S. Weber, C. R. Timmel and P. J. Hore, *Proc. Natl. Acad. Sci.*, 2012, **109**, 4774–4779.
- 16 E. W. Evans, C. A. Dodson, K. Maeda, T. Biskup, C. J. Wedge and C. R. Timmel, *Interface Focus*, 2013, **3**, 20130037–20130037.
- 17 T. M. Zollitsch, L. E. Jarocha, C. Bialas, K. B. Henbest, G. Kodali, P. L. Dutton, C. C. Moser, C. R. Timmel, P. J. Hore and S. R. Mackenzie, *J. Am. Chem. Soc.*, 2018, **140**, 8705–8713.
- 18 C. Bialas, L. E. Jarocha, K. B. Henbest, T. M. Zollitsch, G. Kodali, C. R. Timmel, S. R. Mackenzie, D. W. MacKenzie, P. L. Dutton, C. C. Moser and P. J. Hore, *J. Am. Chem. Soc.*, 2016, **138**, 16584–16587.
- 19 D. M. W. Sheppard, J. Li, K. B. Henbest, S. R. T. Neil, K. Maeda, J. Storey, E. Schleicher, T. Biskup, R. Rodriguez, S. Weber, P. J. Hore, C. R. Timmel and S. R. Mackenzie, *Sci. Rep.*, 2017, **7**, 42228.
- 20 C. C. Moser, M. M. Sheehan, N. M. Ennist, G. Kodali, C. Bialas, M. T. Englander, B. M. Discher and P. L. Dutton, *Meth. Enzymol.*, 2016, **580**, 365–388.
- 21 S. W. Englander, D. B. Calhoun and J. J. Englander, *Anal. Biochem.*, 1987, **161**, 300–306.
- 22 X. Yu, S. Eymur, V. Singh, B. Yang, M. Tonga, A. Bheemaraju, G. Cooke, C. Subramani, D. Venkataraman, R. J. Stanley and V. M. Rotello, *Phys. Chem. Chem. Phys.*, 2012, **14**, 6749.
- 23 E. R. Henry and J. Hofrichter, *Meth. Enzymol.*, 1992, **210**, 129–192.
- 24 G. Puxty, M. Maeder and K. Hungerbühler, *Chemom. Intell. Lab. Sys.*, 2006, **81**, 149–164.
- 25 E. G. Moore, S. Ghisla and V. Massey, *J. Biol. Chem.*, 1979, **254**, 8173–8178.
- 26 R. J. Stanley, *Antioxid. Redox Sig.*, 2001, **3**, 847–866.
- 27 A. Karen, M. T. Sawada, F. Tanaka and N. Mataga, *Photochem. Photobiol.*, 1987, **45**, 49–53.
- 28 Y.-T. Kao, C. Tan, S.-H. Song, N. Öztürk, J. Li, L. Wang, A. Sancar and D. Zhong, *J. Am. Chem. Soc.*, 2008, **130**, 7695–7701.
- 29 J. Brazard, A. Usman, F. Lacombat, C. Ley, M. M. Martin, P. Plaza, L. Mony, M. Heijde, G. Zabulon and C. Bowler, *J. Am. Chem. Soc.*, 2010, **132**, 4935–4945.
- 30 D. Immeln, A. Weigel, T. Kottke and J. L. Perez Lustres, *J. Am. Chem. Soc.*, 2012, **134**, 12536–12546.
- 31 S. Solar, N. Getoff, P. Surdhar, D. Armstrong and A. Singh, *J. Phys. Chem.*, 1991, **95**, 3639–3643.
- 32 C. C. Moser, J. M. Keske, K. Warncke, R. S. Farid and P. L. Dutton, *Nature*, 1992, **355**, 796–802.
- 33 R. J. Stanley and A. W. MacFarlane IV, *J. Phys. Chem. A*, 2000, **104**, 6899–6906.
- 34 G. Li and K. D. Glusac, *J. Phys. Chem. A*, 2008, **112**, 4573–4583.
- 35 W. Holzer, A. Penzkofer, M. Fuhrmann and P. Hegemann, *Photochem. Photobiol.*, 2002, **75**, 479–487.
- 36 J. T. M. Kennis, S. Crosson, M. Gauden, I. H. M. Stokkum, K. Moffat and R. van Grondelle, *Biochem.*, 2003, **42**, 3385–3392.
- 37 H. Li, T. B. Melø and K. R. Naqvi, *J. Photochem. Photobiol., B*, 2012, **106**, 34–39.
- 38 C. Bonetti, T. Mathes, I. H. M. van Stokkum, K. M. Mullen, M. L. Groot, R. van Grondelle, P. Hegemann and J. T. M. Kennis, *Biophys. J.*, 2008, **95**, 4790–4802.
- 39 B. J. G. Rousseau, S. Shafei, A. Migliore, R. J. Stanley and D. N. Beratan, *J. Am. Chem. Soc.*, 2018, **140**, 2853–2861.
- 40 W. Lee, G. Kodali, R. J. Stanley and S. Matsika, *Chem. Eur. J.*, 2016, **22**, 11371–11381.
- 41 D. R. Kattnig, I. A. Solov'yov and P. J. Hore, *Phys. Chem. Chem. Phys.*, 2016, **18**, 12443–12456.
- 42 S. Krapf, S. Weber and T. Koslowski, *Phys. Chem. Chem. Phys.*, 2012, **14**, 11518–7.
- 43 Y. M. Gindt, E. Vollenbroek, K. Westphal, H. Sackett, A. Sancar and G. T. Babcock, *Biochem.*, 1999, **38**, 3857–3866.
- 44 T. Todo, *Mutation Research-Dna Repair*, 1999, **434**, 89–97.
- 45 P. Müller and M. Ahmad, *J. Biol. Chem.*, 2011, **286**, 21033–21040.
- 46 Z. Liu, C. Tan, X. Guo, J. Li, L. Wang, A. Sancar and D. Zhong, *Proc. Natl. Acad. Sci. U.S.A.*, 2013, **110**, 12966–12971.
- 47 A. A. Lee, J. C. S. Lau, H. J. Hogben, T. Biskup, D. R. Kattnig and P. J. Hore, *J. Roy. Soc. Interface*, 2014, **11**, 20131063–20131063.

- 48 T. Biskup, B. Paulus, A. Okafuji, K. Hitomi, E. D. Getzoff, S. Weber and E. Schleicher, *J. Biol. Chem.*, 2013, **288**, 9249–9260.
- 49 S. Weber, C. Kay, H. Mogling, K. Mobius, K. Hitomi and T. Todo, *Proc. Natl. Acad. Sci. U.S.A.*, 2002, **99**, 1319–1322.
- 50 S. Oldemeyer, S. Franz, S. Wenzel, L.-O. Essen, M. Mittag and T. Kottke, *J. Biol. Chem.*, 2016, **291**, 14062–14071.

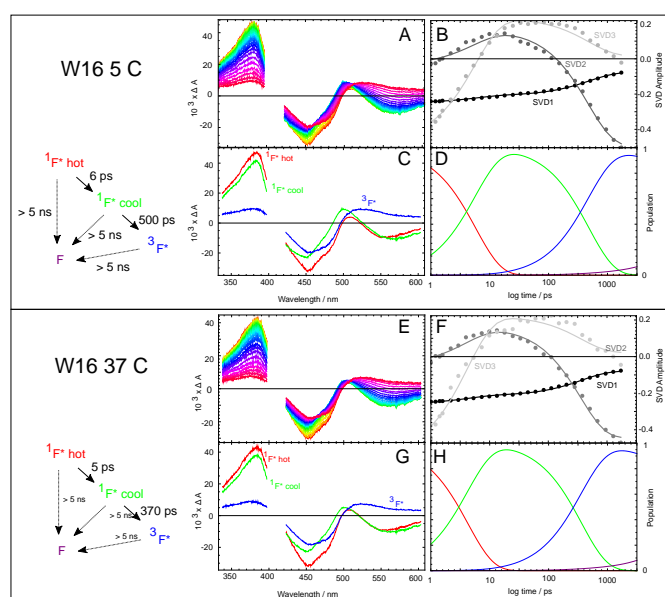
Supporting Information



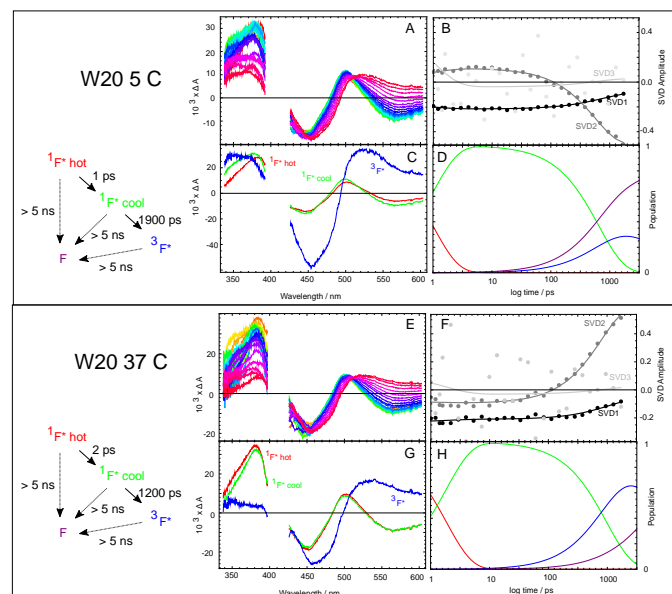
Supplementary Fig. 1 Singular value amplitudes of flavomaquette light-activated kinetics. The dashed line indicates noise components. Two to three components are usefully above the noise level for analysis.



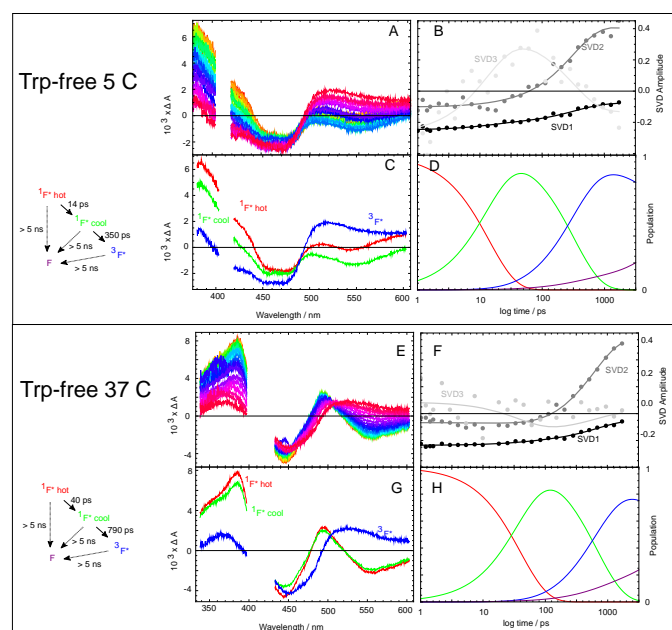
Supplementary Fig. 2 SVD global analysis fit to a four-state sequential model for W13. A) The sequential kinetics model with fit time kinetic time constants. Fluorescence and phosphorescence rates are not well defined on this timescale. B) Log time dependence of three principal SVD components (circles) and their fits to the kinetic model (lines). Reduced $\chi^2 = 3.1$. C) Model fit difference spectra relative to the ground state: hot excited singlet ($^1F^*$ hot; red), the vibrationally cooled excited singlet ($^1F^*$ cool; green) and triplet ($^3F^*$; blue) states. D) Time course of the model populations.



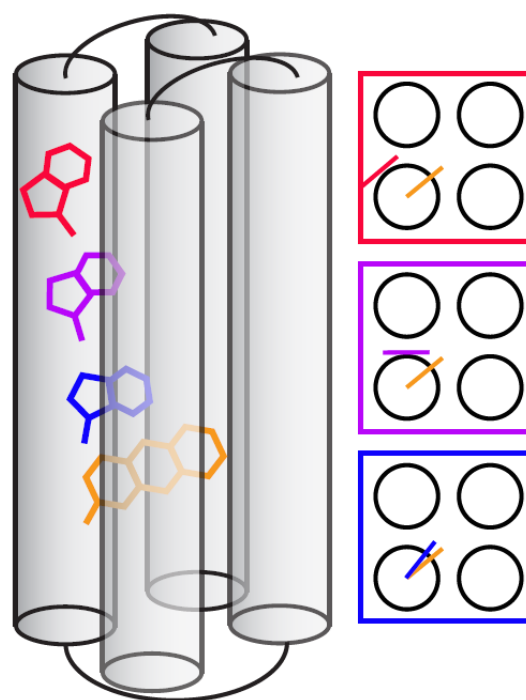
Supplementary Fig. 3 SVD analysis of W16 according to a serial model two temperatures. Top A-D) W16 at 5 °C, Bottom E-H) W13 at 37 °C Left Panels) The elementary sequential kinetic model used to fit W13. A,E) The time resolved spectra used for fitting. B,F) The time evolution of the amplitude of the three SVD spectral components (dots) with the parallel kinetic model fits (lines). C,G) The model-derived spectra of the hot excited singlet ($^1F^*$ hot; red), the vibrationally cooled excited singlet ($^1F^*$ cool; green) and triplet ($^3F^*$; blue) states. D,H) Model population of the three states in log time. The trace colors are the same as in panels C and G and include the ground state F, in purple



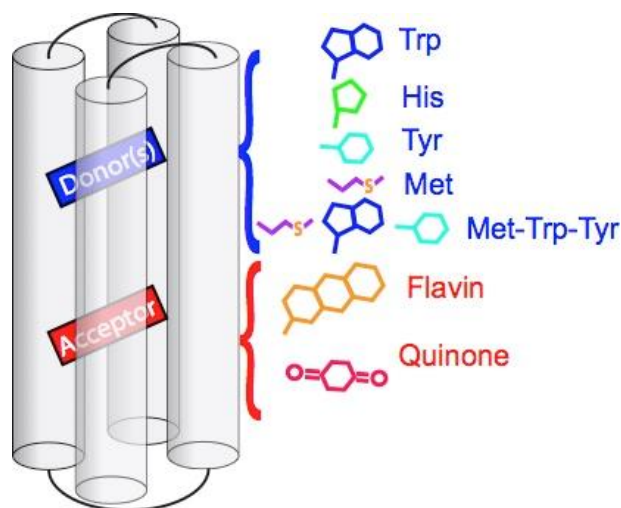
Supplementary Fig. 4 SVD analysis of W20 according to a serial model two temperatures. Top A-D) W16 at 5 °C, Bottom E-H) W16 at 37 °C Left Panels) The elementary sequential kinetic model used to fit W13. A,E) The time resolved spectra used for fitting. B,F) The time evolution of the amplitude of the three SVD spectral components (dots) with the parallel kinetic model fits (lines). C,G) The model-derived spectra of the hot excited singlet ($^1F^*$ hot; red), the vibrationally cooled excited singlet ($^1F^*$ cool; green) and triplet ($^3F^*$; blue) states. D,H) Model population of the three states in log time. The trace colors are the same as in panels C and G and include the ground state F, in purple.



Supplementary Fig. 5 SVD analysis of the Trp-free maquette according to a serial model at two temperatures. Top A-D) Trp-free maquette at 5 °C, Bottom E-H) Trp-free maquette at 37 °C Left Panels) The elementary sequential kinetic model used to fit W13. A,E) The time resolved spectra used for fitting. B,F) The time evolution of the amplitude of the three SVD spectral components (dots) with the parallel kinetic model fits (lines). C,G) The model-derived spectra of the hot excited singlet ($^1F^*$ hot; red), the vibrationally cooled excited singlet ($^1F^*$ cool; green), and triplet ($^3F^*$; blue) states. D,H) Model population of the three states in log time. The trace colors are the same as in panels C and G and include the ground state F, in purple.



Supplementary Fig. 6 Schematic representations of a flavomaquette incorporating three tryptophans (Left). The tryptophan (blue) closest to the flavin (orange) is buried by attachment to a helical “a” or “d” position, the second (purple) is interfacial by attachment at a “b” or “g” position and the third (red) is exposed by attachment to a “c” or “f” position. The increasing solvent exposure produces a ~200 mV redox gradient to promote singlet electron transfer and suppress charge recombination. Right) a plan view of maquette cross section at each tryptophan highlighting tryptophan solvent exposure.



Supplementary Fig. 7 Schematic representations of alternative radical pair generating maquette designs. Potential electron acceptors include flavins or quinones. Potential donors include single amino acids tryptophan, histidine, tyrosine, methionine. Combinations of amino acids are useful in constructing a redox gradient to favor radical pair formation and suppress recombination. Different distance between the initial donor and acceptor will determine initial radical pair spin multiplicity.